LASER & PHOTONICS REVIEWS
www.lpr-journal.org

Suppressing Side-Scattering on Laser-Written Bragg Gratings for Back-Reflection Engineering in Fibers

Jiacheng Hu, Yuying Wang, Kuen Yao Lau, Xuhu Han, Sergei Firstov, Lijing Zhong, Yiping Wang, and Jianrong Qiu**

Laser direct writing (LDW) is versatile in structuring fibers with micro-sized functional elements such as fiber Bragg grating (FBG) and backscattering centers by finely manipulating back and side scattering from laser-induced refractive index modified (RIM) points. However, the side-scattering is a lesser-explored property in laser-structured fibers. In this work, a concise physical model is established to understand the side-scattering as a combined effect of microstructure and geometry of RIM points. Based on a single-pulsed LDW method, the parametric decoupling between scattering loss (α) and coupling strength (κ) coefficients of FBGs is reported, whose cross-section is customized to have a flattened ellipse with thoroughly positive RIM, enabling controllable reflectivity from −21.33 dB to −0.0018 dB while maintaining narrow bandwidth and low loss. Exemplarily, a designed FBG realizes ultra-low loss of 0.008 dB with a resonance attenuation of 10.81 dB, exhibiting a record-breaking κ/α of 2083. Using this FBG as the high-reflective mirror of a home-made bismuth-doped fiber laser, narrow-band lasing with a high optical signal-to-noise ratio of ≈43 dB is achieved, demonstrating flexibilities of the proposed approach in customizing both back- and side-scattering in fibers and opening up wide opportunities for combining multifunctional components into optical fibers and realizing all-fiber networks.

1. Introduction

Optical Bragg gratings, including fiber Bragg gratings (FBG) and distributed Bragg reflectors, are necessary to enable narrow-band filtering and reflection in fiber optical systems[1] and photonic integrated circuits.[2] Categorically, strong Bragg gratings permanently imprint high refractive index changes in the fiber core, allowing efficient enhancement of reflectivity at specified wavelengths for filtering applications,[3] as well as the development of fiber laser mirrors or dispersion compensators.[4] In contrast, ultra-weak Bragg gratings periodically inscribe weak index modification in the core, resulting in ultra-low back-reflection or back-scattering of guided light,[5] which makes the ultra-weak FBG array attractive for building large-scale and real-time quasi-distributed sensing networks by significantly reducing the crosstalk and spectral distortion caused by multiple reflections.[5,6] In addition to harmonic back-reflection or back-scattering, Bragg gratings are capable of scattering light laterally out of the core,[7] causing leakage-mode loss or excitation of cladding modes, especially at tilted Bragg gratings.[8] In most applications of FBG, the side-scattering is a lesser-explored property and is generally considered to be an undesirable optical loss that can significantly deteriorate its overall performance, such as broadening the bandwidth and increasing the frequency noise of strong FBG-based fiber lasers,[9] as well as reducing signal-to-noise ratio and limiting the total interrogation length of ultra-weak FBG-based distributed fiber sensors.[10] Recently, there has been growing interest in exploring the side-scattering, with the goal of developing FBGs into a variety of in-fiber devices, such as spectrometers,[11] line illumination sources,[7a] nanostructured sensors,[12] and polarization filters.[13] Therefore, it is highly relevant to manipulate back- and side-scattering of FBGs for integrating multifunctional components into optical fibers and realizing all-fiber networks. For this purpose, this work delineates a viable method to tailor the refractive index and cross-sectional shape of individual modification points, as well as to finely control the longitudinal period and harmonic reflections of gratings with the help of astigmatic laser pulses at an ultra-stable repetition rate.

J. Hu, Y. Wang, K. Y. Lau, X. Han, J. Qiu
State Key Laboratory of Modern Optical Instrumentation
College of Optical Science and Engineering
Zhejiang University
Hangzhou 310027, China
E-mail: qjr@zju.edu.cn

S. Firstov
Prokhorov General Physics Institute of the Russian Academy of Sciences
Dianov Fiber Optics Research Center
38 Vavilov St., Moscow 119333, Russia

L. Zhong, J. Qiu
Institute of Light+X Science and Technology
College of Information Science and Engineering
Ningbo University
Ningbo 315211, China
E-mail: zhonglijing@nbu.edu.cn

Y. Wang
Shenzhen Key Laboratory of Photonic Devices and Sensing Systems for Internet of Things
College of Physics and Optoelectronic Engineering
Shenzhen University
Shenzhen 518060, China

The ORCID identification number(s) for the author(s) of this article can be found under https://doi.org/10.1002/lpor.202400303

DOI: 10.1002/lpor.202400303

There is a new round of development in the manufacturing technology of Bragg gratings[14] and back-scattering points,[15] with the advent of visible and infrared femtosecond pulsed lasers. Due to the nonlinear absorption of tightly focused fs laser pulses, it becomes possible to modify the refractive index inside the volume of non-photosensitive materials, including silica glass fibers,[15] and sapphire single-crystal fibers[16] by femtosecond laser direct writing (LDW) technique.[17] LDW is a phase mask-free method, which allows the grating structure to be flexibly designed by controlling the focus intensity distribution and scanning scheme with high spatial resolution.[18] To write FBGs, LDW commonly adopts Point-by-Point (P-b-P) and Line-by-Line (L-b-L) schemes. A high numerical aperture (NA) immersion objective is required in P-b-P methods to correct the asymmetry of the cross-section in the refractive index modification (RIM) region, making the RIM region smaller than the core diameter and causing large broadband losses due to Mie scattering.[19] For L-b-L methods, point-shaped traces are replaced with line-shaped traces, which can effectively enhance the coupling coefficient and reduce the scattering loss due to increased area of RIM in the core.[20] Recently, a Plane-by-Plane (Pl-b-Pl) method has attracted great attention due to its flexibility combining the advantages of P-b-P and L-b-L methods that can realize L-b-L modification through simple P-b-P scanning.[21] In one way, Pl-b-Pl creates a rectangular RIM region covering the entire core by elongating the laser-induced modification region based on the laser filamentation effect[22] or spherical aberration enhancement,[11,23] thereby obtaining a large coupling strength coefficient (κ) of 3177.6 m^{-1}.[23] In the other way, Pl-b-Pl method employed slit-shaping[24] or cylindrical lenses[25] to transform the Gaussian beam into an astigmatic beam, which can also expand the RIM area and achieve a strong type-II FBG with a κ value of 1342.7,[26] as well as a type-I FBG with a κ value of 357.1.[25a] Thus, the Pl-b-Pl scheme is a fast, accurate, versatile approach to customizing FBGs.

Besides coupling strength, there is another key parameter of scattering loss coefficient (α), which is generally coupled with κ in the form of κ/α, representing the overall performance of FBG.[19a] When fabricating strong FBGs with high coupling coefficient, the intense laser irradiation may cause the generation of cracks or loosely porous structures in the RIM region,[27] leading to a high refractive index change up to 10^{-1},[1b] but resulting in a high loss and a reduced κ/α value of 172.46.[26] Meanwhile, lower laser pulse energy induce moderate RIM of materials densification,[28] with a positive refractive index change down to 10^{-4},[29] enabling a low loss while also reducing the coupling coefficient,[1b] which results in a high κ/α value of ≈1550.[25a] Therefore, there is a trade-off between coupling strength and scattering loss, setting a technique limit to realize low-loss but strong FBGs.

Here, we argue that the coupling relationship between coupling strength and scattering loss is not theoretically necessary but is caused by the fabrication process. A concise numerical model was established to understand the side-scattering on FBGs as a combined effect of microstructure and refractive index profile (shape and distribution) of individual RIM spots. Based on this, we propose a single-pulsed Pl-b-Pl method using astigmatic fs laser pulse trains to control harmonic reflectivity while suppressing side-scattering of FBGs. The transversal cross-section of individual RIM spots of the fabricated FBG is characterized by flat shape and thoroughly positive refractive index change with variable contrast and diameter, thus enabling controllable reflectivity from −21.33 dB to −0.0018 dB while maintaining low scattering loss and narrow reflection band of <0.4 nm. Specifically, a FBG with all-positive RIM region realizes an ultra-low loss of 0.008 dB and a resonance attenuation of 10.81 dB, which exhibits a record-breaking high κ/α value of 2083. Using this FBG as high-reflective mirror of a home-made bismuth-doped fiber laser, we achieve a high optical signal-to-noise ratio (OSNR, ≈43 dB) and narrow-band lasing, demonstrating its flexibility in customizing high-performance FBGs. Consequently, through this approach, the coupling strength and scattering loss of FBGs are technically decoupled, which represents a significant advance in suppression and manipulation of the back-reflectivity and side-scattering of Bragg gratings and back-scattering points by LDW technique.

2. Results and Discussion

2.1. Comparison of FBG Fabrication Schemes and All-Positive RIM FBG

To illustrate our method (method **C**, **Figure 1c**), two conventional P-b-P inscription schemes using an oil immersion objective (method **A**, Figure 1a) and a dry objective (method **B**, Figure 1b) are also demonstrated for comparison. In the setup of the method **A** (Figure 1a), the gap between the optical fiber and the objective was filled with refractive index matching oil (n = 1.476), in order to minimize the interface spherical aberration. For methods **B** and **C**, the fiber was clamped by a 0.2 mm thick quartz coverslip to enhance the spherical aberration (SA) effect,[12,23,25b,30] resulting in a remarkable stretch of the Rayleigh length from 2.3 μm (Figure 1d) to 15.2 μm (Figure 1e) and 17.7 μm (Figure 1f). In our method **C**, in order to enlarge the RIM region in Y-direction and further enhance coupling coefficient (see Section 2.3 for more details), a pair of cylindrical lenses with focal length of 50 mm and 150 mm were placed in the light path to transform the input non-astigmatic beam to an astigmatic one. As depicted in Figure 1f, the focus width in the Y-direction (4.1 μm) is nearly twice larger than that of method **B** (2.0 μm), resulting in a sharp reduction in the peak intensity gradient; Based on our previous study,[31] the damping of peak intensity gradient can suppress the generation of light scattering centers (including cracks, and porous and ripple structures) in the laser irradiated region, leading to an all-positive RIM throughout the laser modified region, such as the fiber core in this work (see Section 2.4 for more details). To compare grating performance, a 4 mm long second-order fiber grating was fabricated using the above three methods (Figure 1g–i). The grating pitch (Δ) was set at 1.071 μm to match the designed wavelength of 1550 nm according to the Bragg resonance equation: $2n\Delta = m\lambda$, where n is the core refractive index, m is the grating order and the λ is the wavelength.

From the top view (Figure 1g), the dark area in the center indicates the presence of micro-voids, which are surrounded by bright areas that are generated due to the densification of the surrounding matter during micro-void formation.[32] These bright regions lead to positive RIM changes.[33] With enhanced SA in method **B** (Figure 1h), a central dark area is also observed, but

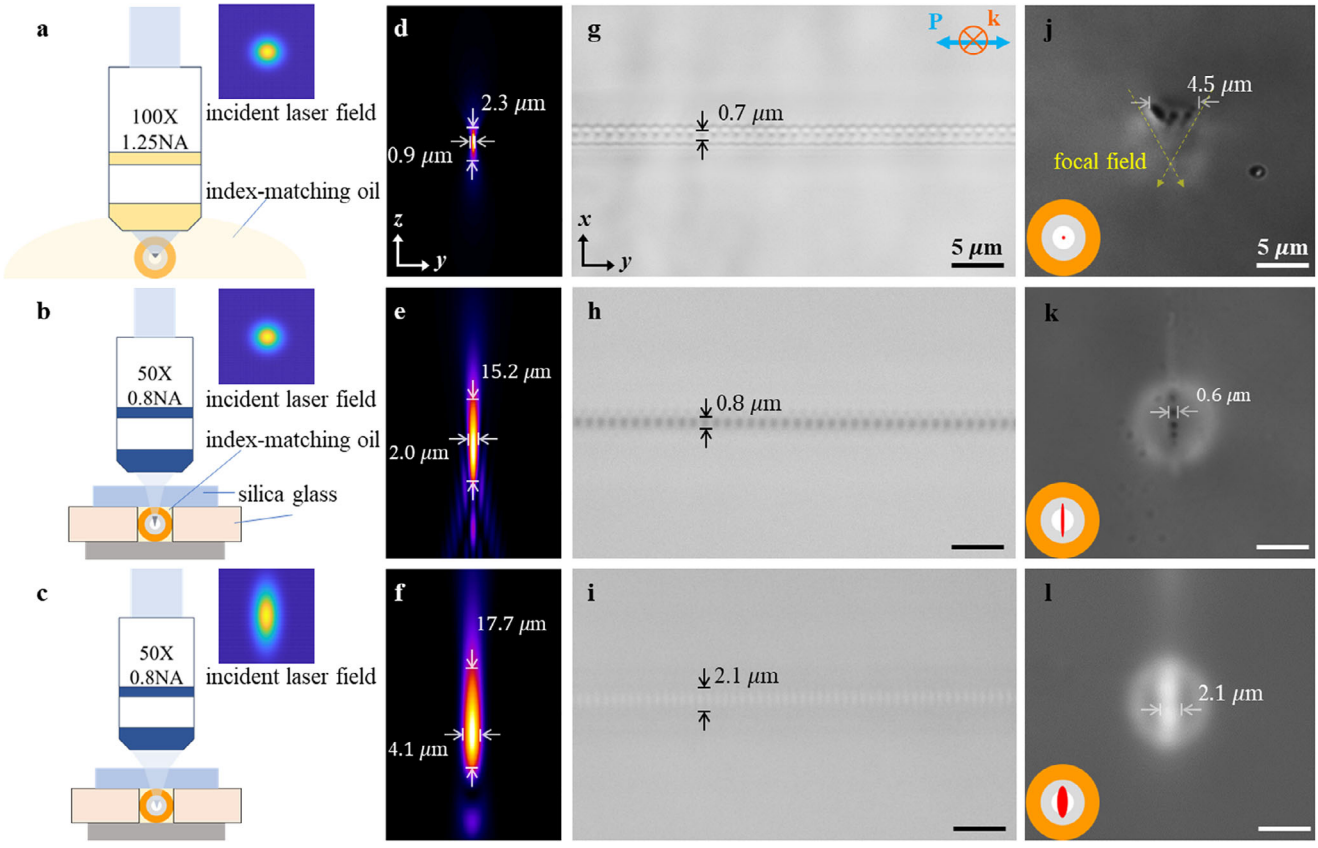

Figure 1. P-b-P schemes using an oil immersion objective (method **A**, row 1) and a dry objective (method **B**, row 2), and Pl-b-Pl scheme using a dry objective and cylindrical lenses (method **C**, row 3). a–c) Schematic diagram of experimental setup for FBG inscription, d–f) simulated intensity distribution in the focus plane, microscope images in the top view g–i) and cross-section j–l). The length of FBGs is 4 mm. The blue arrow in (g) represents the writing beam polarization direction.

the surrounding bright area is reduced which can be attributed to the energy dispersion in the z-direction. In contrast, the RIM region created by the proposed method **C** has a bright RIM region with a width expanded to 2.1 μm (Figure 1i), compared to 0.7 and 0.8 μm in Figure 1g,h, respectively. From the cross-section, the RIM region created with an oil immersion objective is primarily confined to the core (Figure 1j), containing several micro-voids arranged similar to the laser focus pattern. With the same scanning speed but an enhanced SA (Figure 1k), the cross-section of the RIM region exhibits a significant elongation in the Z-direction and spans the entire fiber core with a whole length of >15 μm, which composes of a string of micro-voids in its center, as reported in previous work.[34] It is worth noting that compared to the cladding, the micro-voids mainly appeared in the fiber core (as detailed in Text S1, Supporting Information), indicating that the core has a lower damage threshold compared to the cladding, which can be attributed to the small amount of germanium doping in the fiber core.[35] Therefore, it is crucial to reduce the laser intensity gradient in order to avoid the generation of micro-voids in the fiber core. In the case of method **C**, the trace is also elongated and extended throughout the core; and the incorporation of astigmatic laser beam leads to the expansion of the RIM region. Consequently, a trace of all-positive RIM was created in the cross-section (Figure 1l). The SEM of FBG cross-section provides a clearer visualization of the RIM profile (as detailed in Text S2, Supporting Information), revealing that the positive RIM region substantially increases in FBG cross-sections inscribed by using method **C**, and no central micro-void was observed (Figure S3c and S4, Supporting Information). Thereby, these results demonstrate the feasibility of the suggested method **C** to inscribe structures with all-positive RIM that exclusively penetrates through the core by engineering the laser intensity distribution in the focus volume.

2.2. Side-Light Scattering on FBGs

Side-light scattering of FBGs is a less studied property due to difficulties in both theoretical calculations and experimental measurements in quantifying the side scattered light.[7] Here, a concise physical mode was established for a better understanding of the side-scattering on FBGs as a combined effect of microstructure and refractive index profile (shape and distribution) of individual RIM spots.

Experimentally, it is informative to directly observe the scattering pattern excited by the RIM region by coupling a visible laser beam with a central wavelength of 650 nm into the fiber. Resulting from the periodic RIM in the core, the stable trans-

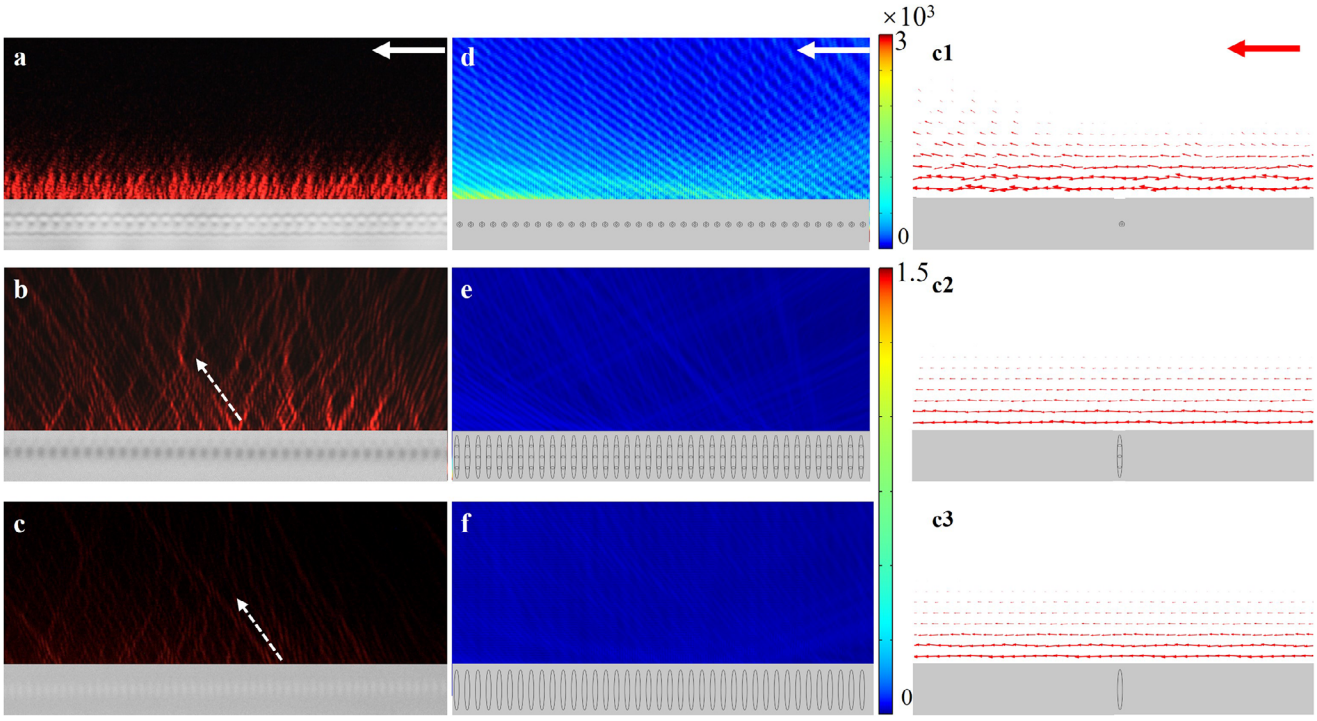

Figure 2. Scattering patterns appearing when a 650 nm laser is incident on FBGs inscribed by method **A** (row 1), method **B** (row 2) and a method **C** (row 3). a–c) Measured and d–f) simulated side-scattered light field of FBGs, and g–i) simulated scattered-light field flux of single RIM spot. The arrows in a, d and g indicate the incident direction of the laser. The dash arrows in b and c represent the major direction of the forward scattering light.

mission mode is coupled with radiation mode and subsequently be leaked and captured by the microscope.[36] In **Figure 2a**, the FBGs inscribed with method **A** display a strong scattering and light leakage phenomena due to the high refractive index contrast of micro-voids. The interference pattern is relatively intensive and chaotic since the multiple micro-voids structures. The micro-voids in FBGs display strong scattering light in all directions and make it impossible to identify the light enhanced at specific angles.[7a] In comparison, the FBG made by method **B** has a more regular RIM area, and the scattered light exhibits periodic interference enhancement (Figure 2b). In the case of method **C**, FBG demonstrates weaker scattering light (Figure 2c). The significant reduction in scattered light intensity allows the observation of the directionality of scattered light. The scattering angles were statistically counted from the microscope images (Figure 2c), similar to the method in the literature.[7a] The results showed that the direction of the forward scattered light was highly concentrated, with a deviation within 0.95 rad. This suggests the dominance of low-order harmonics (radiation modes in coupled-mode theory[37]), which is consistent with numerical calculations of first-order harmonics using the volume-current method.[7] In addition, a small amount of high-order harmonics are excited and cause backward scattering (Figure 2a–c), which can be attributed to the slight deviations from the standard sinusoidal refractive index distribution.[1c,38] In general, the presence of harmonics will conspicuously increase the cladding-mode loss in the range of short wavelength and impact the multiplexing capability of FBGs.[39] As discussed in Section 2.3, method **C** can significantly reduce the short-wavelength loss of FBG by suppressing the generation of harmonics, which is expected to dramatically improve the performance of optical systems containing FBG.

Numerically, three types of FBGs were simulated by commercial finite element analysis software COMSOL, where the structures of RIM traces are reasonably simplified to represent RIM profiles in different methods based on corresponding experimental results (Figure 1). The details of simulation structures are discussed in Text S3 (Supporting Information). In the FBG written by method **A** (Figure 2d), with micro-sized voids in the center, strong scattering was observed with a large amount of near-field Mie scattering light appeared in forward and backward directions similar with that reported in the literature,[32b] resulting in a large transmission loss of 2.017 dB. In the FBG written by method **B** (Figure 2e), the scattering light is weaker with lower transmission loss of 0.184 dB, indicating that the enlarged RIM region can efficiently reduce the transmission loss despite the presence of micro-voids in the center. In the case of method **C** with all-positive RIM, the transmission loss is merely 0.0109 dB, only forward scattering can be distinguished (as shown in Figure 2f) and the scattered light intensity drops by an order of magnitude.

Additionally, the scattering pattern of individual RIM spots in fiber were also calculated (Figure 2g–i and Figure S6, Supporting Information). For the RIM spot created by method **A**, the scattered light field undergoes significant torsion and exhibits a substantial angular deviation at the core-cladding boundary (Figure 2g and the light field distribution in Figure S6, Supporting Information). When an all-positive RIM spot presents in the core by method **C**, the light field disturbance at boundary is much smaller (Figure 2i); and the light field distribution ap-

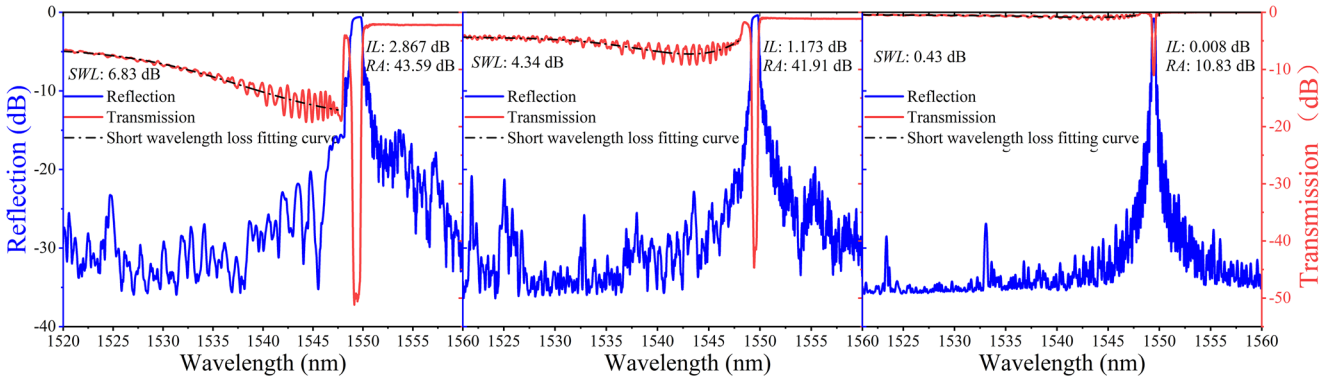

Figure 3. Reflection and transmission spectrum of FBGs inscribed by using a) method **A**, b) method **B**, and c) method **C**. *SWL*: short-wavelength loss. *IL*: insert loss. *RA*: resonance attenuation.

pears uniform and exhibits minimal scattering effects. The scattering losses of the three individual RIM spots (Figure 2g–i) are 0.048 dB, 0.00017 dB, and 0.000087 dB, respectively, exhibiting a strong correlation on the dependence of scattering loss on the RIM profile. Therefore, whether in the case of single RIM spot or periodic grating, the all-positive RIM is demonstrated to possess a distinct advantage for suppressing scattering loss. Meanwhile, in analytic theory as detailed in Text S4 (Supporting Information), the Rayleigh scattering is an approximation of Mie scattering, assuming that the scatterer diameter is much smaller than the wavelength. With an extended all-positive RIM that we created with method **C**, whose diameter is comparable to or larger than the wavelength, the Rayleigh scattering approximation becomes inadequate and it is necessary to employ the Mie scattering formula. Notably, unlike Rayleigh scattered light, which has no preferential directionality, most of the Mie scattered light propagates forward and has a small angular deviation,[40] making it easy to be collected and confined by the core-cladding structure of the optical fiber. The confinement effect of the optical fiber can not only effectively reduce the scattering loss, but also increase the coherence length of the periodically distributed RIM spots, thereby enhancing the coupling coefficient of the FBG.[41] Moreover, the coupling relationship between coupling strength and scattering loss is not theoretically necessary, and it is possible to achieve a parametric decoupling as detailed in Text S7 (Supporting Information).

2.3. Characteristics of Fabricated FBGs

The spectral characteristics of FBGs inscribed three methods were shown in **Figure 3**. In Figure 3a,b, both FBGs containing micro-voids exhibit a strong Bragg resonance attenuation of over 40 dB (a reflectivity higher than 99.99%) near the wavelength of 1550 nm in the transmission spectra. However, they also demonstrate a high insertion loss up to 2.86 dB and 1.17 dB, resulting in a low κ/α value of merely 17.30 and 40.86, respectively. Due to the discrete radiation modes, the short-wavelength loss (SWL) exhibited strong oscillations, to achieve better quantitative measurement, we fit the SWL to a smooth curve. FBG inscribed by method **A** displayed a high *SWL* up to 6.83 dB due to the highly localized RIM regions and non-uniform refractive index profile in the cross-section plane.[39] For FBG inscribed by method **B**, the *SWL* is reduced to 4.34 dB but maintained at a high level. In method **C**, due to all-positive RIM, the FBG shows a relatively low resonance attenuation of 10.83 dB and an ultra-low insertion loss of 0.008 dB, resulting in a much higher κ/α value of 2083 (as detailed in Text S7, Supporting Information). Meanwhile, its *SWL* is significantly suppressed to 0.43 dB, which is in good agreement with the light scattering analysis of the lower harmonics presented in Section 2.2.

2.4. Controlling Reflectivity of FBGs

Furthermore, it is demonstrated that reflectivity can be controlled by manipulating the refractive index profile of FBGs. For the energy <1.2 μJ, the FBGs featuring an all-positive RIM region demonstrate ultra-low insertion loss and relatively low resonance attenuation. In the core area, it is hard to identify the RIM region because of the limited modification area and the low RI change in **Figure 4**a. As the pulse energy increases to greater than 2 μJ (Figure 4b,c), the RIM regions in the y-direction were enlarged to 5.1 μm. Eventually, they created RIM regions that cover almost the entire core without overlap of adjacent traces in the cross-section, as correspondingly shown in Figure 4d–f. The RIM region only appears in the core area at low pulse energy of 0.9 μJ (Figure 4d), but expands along the transverse and longitudinal directions as the pulse energy increases (Figure 4e,f). Consequently, the expansion of the FBG cross-section width allows its reflectivity to be controllably increased from −0.86 dB to −21.33 dB (Figure 4g), while maintaining a narrow bandwidth of <0.4 nm and negligible loss (<0.001 dB).

Ultra-weak FBG arrays, as a promising solution for quasi-distributed sensing, present numerous advantages, including significantly higher OSNR compared to traditional sensing schemes.[1a,42] To date, there are few reports on the fabrication of ultra-weak FBGs by using a femtosecond laser. Xu et al.[43] reported for the first time a new method for fabricating ultra-weak FBGs based on a P-b-P technology, in which the pulse energy and the length of the FBG were precisely regulated to reach an ultra-low reflectivity. Our Pl-b-Pl inscription technology also enables the inscription of high-quality ultra-weak

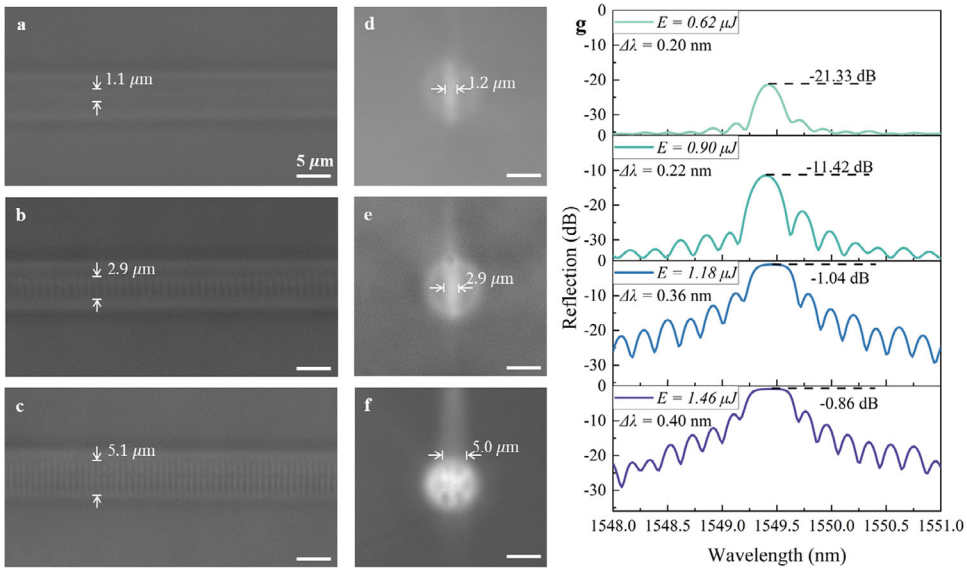

Figure 4. a–c) Top view and d–f) cross-section view microscope images of Pl-b-Pl FBGs inscribed with different pulse energies of 0.90 μJ (row 1), 2.02 μJ (row 2), and 2.86 μJ (row 3), g) reflection spectra of FBGs inscribed with different pulse energies *E*. Δλ: bandwidth, which is measured at positions that 3 dB lower than the peak in reflection.

FBGs with controllable reflectivity and narrow bandwidth. The lowest reflectivity of −21.33 dB was achieved at the pulse energy of 0.62 μJ (Figure 4g), indicating a lower coupling coefficient of 20.3 m^{-1} and a much narrower bandwidth compared to the reference.[43] In fact, small RIM area and low index change are challenging to achieve using traditional P-b-P method.[19b,24b,26] The insertion loss of the ultra-weak FBG remains within our margin of measurement error, can be disregarded (<0.001 dB). By increasing pulse energy, a trend of broadening of the bandwidth is observed. This phenomenon is believed to be attributed to the intrinsic characteristics of FBGs by coupled-mode theory.[19a] For weak FBGs that light penetrate the full length of the grating, the bandwidth is proportional to the length of the FBGs (fundamentally, the cycles number of the FBGs).

2.5. Application: Narrowband Bismuth-Doped Fiber Laser

To demonstrate the general applicability of method **C**, a similar FBG was inscribed to an Hi1060 single mode fiber (Corning), which has a smaller core size (5.3 μm). Combining with bismuth-doped aluminosilicate fiber (BASF), we demonstrate an all-fiber laser with high OSNR (≈43 dB) and adjustable central wavelength. A schematic diagram of the experimental setup for the fiber laser is presented in **Figure 5**a,b with fiber mirror (FM) and homemade FBG, respectively. In both cases, a 1064 nm single-mode laser diode (LD) acts as a pump source for the BASF with connection through a 1064/1160 nm wavelength division multiplexer (WDM-1). The residual pump (RP) at 1064 nm was extracted from the laser cavity via another 1064/1160 nm wavelength division multiplexer (WDM-2). In Figure 5a, two FMs

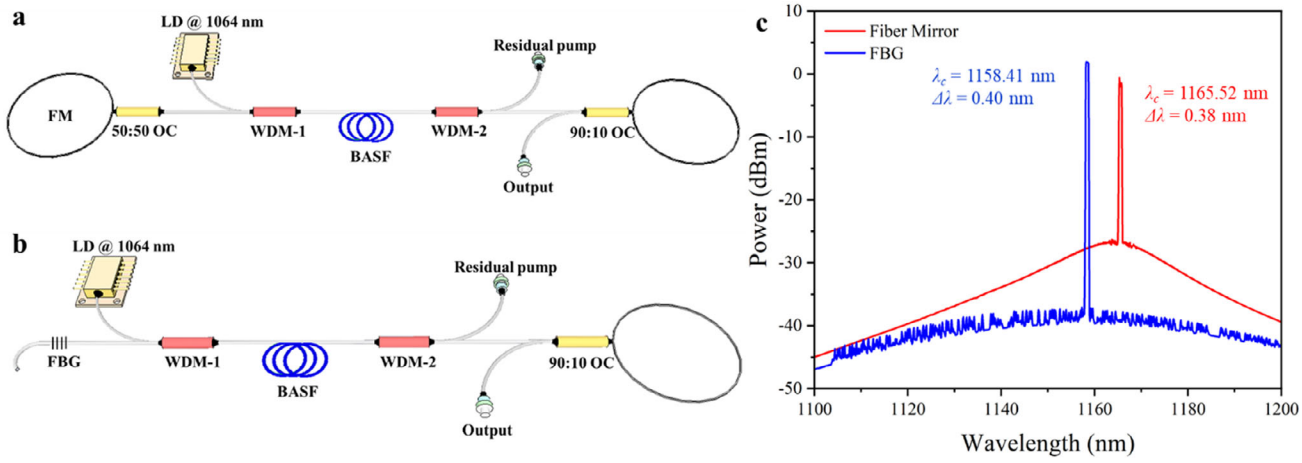

Figure 5. a) Experimental setup for bismuth-doped fiber laser with fiber mirror and b) homemade FBG, c) output spectrum of the fiber laser with the fiber mirror or homemade FBG, respectively.

were constructed from a 50:50 optical coupler (OC) and a 90:10 OC. The laser output (OP) was measured through the 10% port of the 90:10 OC, while the remaining 90% of the laser signal returned to the laser cavity. With optimized parameters, we successfully inscribed FBG with a designed wavelength of 1160 nm as a high-reflective mirror in all-fiber laser to replace conventional FM.

The output spectrum of the fiber lasers, whether equipped with a fiber mirror or a homemade FBG, exhibits significant disparities in both OSNR and central wavelength (Figure 5c). The implementation of FBG significantly increase the OSNR due to its bandpass characteristics and the low insertion loss that effectively mitigates parasitic lasing and concentrates energy on the central wavelength (i.e., OSNR for fiber mirror and FBG was measured to be ≈43 dB and ≈25 dB, respectively). In the case of FM utilization, a peak power is observed at 1165.52 nm as a result of the optical transition from bismuth-related active center.[44] The laser equipped with FBG, however, exhibits a blue-shifting in central wavelength, which is determined by the FBG reflection peak wavelength. The wavelength of a customizable laser can be adjusted by modifying the period of the FBG through variations in stress or temperature,[45] making it highly practical for implementation in optical communications[46] and fiber sensing.[20b,47]

3. Conclusion

In summary, we achieve the decoupling of scattering loss and coupling strength in FBGs by adjusting the refractive index profile through the introduction of an astigmatic beam and an enlarged SA. Based on this, we propose an innovative Pl-b-Pl inscription technology for the fabrication of low-loss FBGs. The side-scattering and harmonic reflectivity of the FBG can be effectively controlled through the customization of cross-sectional shape and refractive index distribution. By shaping individual modified points and customizing structural modifications, we achieve fine adjustment of FBGs reflectivity, ranging from ultra-weak FBGs to strong FBGs. Additionally, the optimized refractive index profile facilitates the inscription of high-quality FBG with an exceptionally low loss of 0.008 dB, exhibiting a record-breaking high κ/α value of 2083. The proposed Pl-b-Pl method has general applicability that allows for extension to specific fibers, and facilitates the realization of an all-fiber laser with a customizable central wavelength and a narrow linewidth. This work is highly relevant not only for the fabrication of high-performance FBGs but also for the creation of multifunctional fiber-optic platforms integrating communication, modulation,[13] distributed sensing,[48] 3D imaging[49] and large-area illumination[7b] based on LDW method.

4. Experimental Section

In the experiment, a high-repetition-rate chirped pulse amplified femtosecond Yb: KGW laser source (Pharos, Light Conversion) that generates pulses with a duration of 213 fs, a central wavelength of 1030 nm, and an adjustable repetition rate ranging from 200 Hz to 1 MHz was used. The single mode fiber (YOFC, G652D) was moved at a constant velocity (1.071 mm $^{-1}$s with a constant repetition rate of 1000 Hz, served to align with the characteristic wavelength of 1550 nm) using a high-accuracy 3-D air bearing stage (Aerotech). The scanning process is similar to the P-b-P method, in order to achieve high effective inscribing. To study the micrographs and microstructure of the FBG cross-section, the optical fiber was cut at the FBG cross-section and polished to optical mirror smoothness. Optical microscope (OM, Olympus) and scanning electron microscope (SEM, Carl Zeiss) were employed to observe the morphology of the RIM regions. An oil immersion objective (Nikon, 100×, 1.25 NA) and a dry objective (Nikon, 50×, 0.8 NA) were adopted to focus the laser beam at the core in different methods. The FBGs were monitored by utilizing a broadband laser (MC Fiber Optics) and an optical spectrum analyzer (OSA, Yokogawa). We calculated the intensity distribution at the focus plane using a numerical method.[50] The single-mode Bismuth-doped fiber was drawn from a preform produced by the modified chemical vapor deposition (MCVD) process[51] with an outer diameter of 125 µm and a cut-off wavelength of ≈1000 nm. To meet the central wavelength of 1160 nm, the repetition rate was set at 1000 Hz and the velocity was set at 0.802 mm $^{-1}$s. (The refractive index of the core of the Bismuth-doped fiber is assumed to be equivalent to that of G652D fiber).

The spectral characteristics of FBGs were monitored by utilizing an amplified spontaneous emission source (ASE) (MC Fiber Optics) that passed through an optical circulator (Figure S7, Supporting Information), the transmission and reflection spectra were recorded using an optical spectrum analyzer (OSA, Yokogawa). The insertion loss (T_{IL}) is measured at 1560 nm to eliminate interference from cladding modes loss. Similarly, the short-wavelength loss (*SWL*) is measured at 1520 in a fitting curve to eliminate the impact of periodic oscillations. The transmission and reflection spectra were normalized by comparing that of a blank fiber (Supplementary text S8, Supporting Information).

Supporting Information

Supporting Information is available from the Wiley Online Library or from the author.

Acknowledgements

This work was supported by the National Key Research and Development Program of China (No. 2021YFB2800500) and Zhejiang Provincial Natural Science Foundation (No. LQ22F050022).

Conflict of Interest

The authors declare no conflict of interest.

Data Availability Statement

The data that support the findings of this study are available in the supplementary material of this article.

Keywords

fiber Bragg grating, fiber laser, laser direct writing, side scattering

Received: March 6, 2024
Revised: July 5, 2024
Published online:

[1] a) P. Lu, N. Lalam, M. Badar, B. Liu, B. T. Chorpening, M. P. Buric, P. R. Ohodnicki, *Appl. Phys. Rev.* **2019**, *6*, 041302; b) J. He, B. Xu, X. Xu, C. Liao, Y. Wang, *Photonic Sens.* **2021**, *11*, 203; c) J. Thomas, C. Voigtländer, R. G. Becker, D. Richter, A. Tünnermann, S. Nolte, *Laser Photonics Rev.* **2012**, *6*, 709.

[2] Y. Wang, J. A. Holguín-Lerma, M. Vezzoli, Y. Guo, H. X. Tang, *Nat. Photonics* **2023**, *17*, 338.
[3] A. Othonos, *Rev. Sci. Instrum.* **1997**, *68*, 4309.
[4] a) J. Dong, K. S. Chiang, *IEEE Photonics Technol. Lett.* **2014**, *26*, 1766; b) G. Bai-Ou, T. Hwa-Yaw, L. Sien-Ting, H. L. W. Chan, *IEEE Photonics Technol. Lett.* **2005**, *17*, 169.
[5] A. Wolf, A. Dostovalov, K. Bronnikov, M. Skvortsov, S. Wabnitz, S. Babin, *Opto-Electron. Adv.* **2022**, *5*, 210055.
[6] a) Y. Wang, J. Gong, D. Y. Wang, B. Dong, W. Bi, A. Wang, *IEEE Photonics Technol. Lett.* **2011**, *23*, 70; b) Z. Luo, H. Wen, H. Guo, M. Yang, *Opt. Express* **2013**, *21*, 22799.
[7] a) A. Reupert, I. Chiamenti, M. Chernysheva, L. Wondraczek, *ACS Photonics* **2023**, *10*, 2765; b) A. Reupert, M. Heck, S. Nolte, L. Wondraczek, *Adv. Opt. Mater.* **2020**, *8*, 2000633.
[8] J. Albert, L.-Y. Shao, C. Caucheteur, *Laser Photonics Rev.* **2013**, *7*, 83.
[9] Y. Li, P. Lu, F. Baset, Z. Ou, J. Song, A. Alshehri, V. R. Bhardwaj, X. Bao, *Appl. Phys. Lett.* **2014**, *105*, 101105.
[10] a) S. J. Mihailov, *APL Photonics* **2023**, *8*, 071102; b) Z. Cai, B. Li, Z. Bai, D. Liu, K. Yang, B. Liu, C. Zhao, M. Zou, J. Zhou, S. Jiang, J. Huang, L. Liu, X. Zhang, J. Qu, Y. Wang, C. Liao, *Int. J. Extreme Manuf.* **2023**, *5*, 035502.
[11] A. Rahnama, K. Mahmoud Aghdami, Y. H. Kim, P. R. Herman, *Adv Photonics Res* **2020**, *1*, 2000026.
[12] K. M. Aghdami, A. Rahnama, E. Ertorer, P. R. Herman, *Nat. Commun.* **2021**, *12*, 6344.
[13] A. Rahnama, T. Dadalyan, K. Mahmoud Aghdami, T. Galstian, P. R. Herman, *Adv. Opt. Mater.* **2021**, *9*, 2100054.
[14] A. Martinez, M. Dubov, I. Khrushchev, I. Bennion, *Electron. Lett.* **2004**, *40*, 1170.
[15] B. Redding, M. J. Murray, A. Donko, M. Beresna, A. Masoudi, G. Brambilla, *Opt. Express* **2020**, *28*, 14638.
[16] G. Shi, R. Shurtz, G. Pickrell, A. Wang, Y. Zhu, *Opt. Lett.* **2022**, *47*, 4724.
[17] a) K. Sun, D. Tan, X. Fang, X. Xia, D. Lin, J. Song, Y. Lin, Z. Liu, M. Gu, Y. Yue, J. Qiu, *Science* **2022**, *375*, 307; b) X. Xu, T. Wang, P. Chen, C. Zhou, J. Ma, D. Wei, H. Wang, B. Niu, X. Fang, D. Wu, S. Zhu, M. Gu, M. Xiao, Y. Zhang, *Nature* **2022**, *609*, 496; c) Y. Yang, L. Zhong, Y. Cui, Y. Wang, D. Chen, K. Y. Lau, X. Liu, Z. Ma, G. Barillaro, Z. Chen, J. Qiu, *Nanophotonics* **2023**, *12*, 3069; d) Y. Wang, L. Zhong, K. Y. Lau, X. Han, Y. Yang, J. Hu, S. Firstov, Z. Chen, Z. Ma, L. Tong, K. S. Chiang, D. Tan, J. Qiu, *Light Sci. Appl.* **2024**, *13*, 130.
[18] R. J. Williams, C. Voigtländer, G. D. Marshall, A. Tünnermann, S. Nolte, M. J. Steel, M. J. Withford, *Opt. Lett.* **2011**, *36*, 2988.
[19] a) R. J. Williams, N. Jovanovic, G. D. Marshall, G. N. Smith, M. J. Steel, M. J. Withford, *Opt. Express* **2012**, *20*, 13451; b) R. J. Williams, R. G. Kramer, S. Nolte, M. J. Withford, M. J. Steel, *Opt. Express* **2013**, *21*, 26854; c) N. Jovanovic, J. Thomas, R. J. Williams, M. J. Steel, M. J. Withford, *Opt. Express* **2009**, *17*, 6082.
[20] a) K. Zhou, M. Dubov, C. Mou, L. Zhang, V. K. Mezentsev, I. Bennion, *IEEE Photonics Technol. Lett.* **2010**, *22*, 1190; b) X. Xu, J. He, C. Liao, K. Yang, K. Guo, C. Li, Y. Zhang, Z. Ouyang, Y. Wang, *Opt. Lett.* **2018**, *43*, 4562; c) J. He, Z. Chen, X. Xu, J. He, B. Xu, B. Du, K. Guo, R. Chen, Y. Wang, *Opt. Lett.* **2021**, *46*, 5663.
[21] R. J. Williams, R. G. Kramer, S. Nolte, M. J. Withford, *Opt. Lett.* **2013**, *38*, 1918.
[22] F. Ahmed, M. B. G. Jun, *J Micro Nanomanuf* **2014**, *2*, 021007.
[23] J. Wu, X. Xu, C. Liao, X. Weng, L. Liu, J. Qu, Y. Wang, J. He, *Opt. Express* **2023**, *31*, 3831.
[24] a) P. Roldan-Varona, D. Pallares-Aldeiturriaga, L. Rodriguez-Cobo, J. M. Lopez-Higuera, *J. Lightwave Technol.* **2020**, *38*, 4526; b) A. Theodosiou, A. Lacraz, A. Stassis, C. Koutsides, M. Komodromos, K. Kalli, *J. Lightwave Technol.* **2017**, *35*, 5404.
[25] a) P. Lu, S. J. Mihailov, H. Ding, D. Grobnic, R. B. Walker, D. Coulas, C. Hnatovsky, A. Y. Naumov, *J. Lightwave Technol.* **2018**, *36*, 926; b) J. He, J. Wu, X. Xu, C. Liao, S. Liu, X. Weng, L. Liu, J. Qu, Y. Wang, *J. Lightwave Technol.* **2023**, *41*, 7014; c) P. Luo, F. Chen, X. Li, W. Zhu, W. Bao, R. Wang, X. Qiao, *Opt. Lett.* **2022**, *47*, 3127.
[26] X. Xu, J. He, J. He, B. Xu, R. Chen, K. Yang, C. Liao, Y. Yang, Y. Wang, *J. Lightwave Technol.* **2021**, *39*, 5142.
[27] M. Lancry, B. Poumellec, J. Canning, K. Cook, J.-C. Poulin, F. Brisset, *Laser Photonics Rev.* **2013**, *7*, 953.
[28] C. W. Ponader, J. F. Schroeder, A. M. Streltsov, *J. Appl. Phys.* **2008**, *103*, 063516.
[29] J. Zhao, Y. Zhao, Y. Peng, R.-q. Lv, Q. Zhao, *Opt. Laser Technol.* **2022**, *146*, 107473.
[30] X. Li, F. Chen, W. Bao, R. Wang, X. Qiao, *Opt. Laser Technol.* **2023**, *161*, 109226.
[31] L. Zhong, Y. Wang, D. Tan, J. Qiu, *Laser Photonics Rev.* **2023**, *17*, 2200767.
[32] a) C. Hnatovsky, K. D. Silva, N. Abdukerim, R. B. Walker, H. Ding, S. J. Mihailov, *Opt. Express* **2022**, *30*, 47361; b) T. Qiu, S. Yang, A. Wang, *Opt. Express* **2020**, *28*, 37553.
[33] C. Smelser, S. Mihailov, D. Grobnic, *Opt. Express* **2005**, *13*, 5377.
[34] J. Lu, Y. Dai, Q. Li, Y. Zhang, C. Wang, F. Pang, T. Wang, X. Zeng, *Nanoscale* **2019**, *11*, 908.
[35] Y. Shimotsuma, P. G. Kazansky, J. Qiu, K. Hirao, *Phys. Rev. Lett.* **2003**, *91*, 247405.
[36] a) A. Reupert, M. Heck, S. Nolte, L. Wondraczek, *Opt. Mater. Express* **2019**, *9*, 2497; b) J. U. Thomas, N. Jovanovic, R. G. Kramer, G. D. Marshall, M. J. Withford, A. Tunnermann, S. Nolte, M. J. Steel, *Opt. Express* **2012**, *20*, 21434.
[37] Y. Li, T. G. Brown, *J. Opt. Soc. Am. B* **2006**, *23*, 1544.
[38] S. J. Mihailov, *Opto-Mechanical Fiber Optic Sens.* **2018**, 137.
[39] J. Thomas, N. Jovanovic, R. G. Becker, G. D. Marshall, M. J. Withford, A. Tunnermann, S. Nolte, M. J. Steel, *Opt. Express* **2011**, *19*, 325.
[40] H. C. Van de Hulst, V. Twersky, *Phys. Today* **1957**, *10*, 28.
[41] M. L. Åslund, N. Nemanja, N. Groothoff, J. Canning, G. D. Marshall, S. D. Jackson, A. Fuerbach, M. J. Withford, *Opt. Express* **2008**, *16*, 14248.
[42] C. Li, J. Tang, C. Cheng, L. Cai, M. Yang, *Photonic Sens.* **2021**, *11*, 91.
[43] B. Xu, J. He, B. Du, X. Xiao, X. Xu, C. Fu, J. He, C. Liao, Y. Wang, *Opt. Express* **2021**, *29*, 32615.
[44] a) A. Vakhrushev, A. Umnikov, S. Alyshev, A. Khegai, E. Firstova, L. Iskhakova, A. Guryanov, M. Melkumov, S. Firstov, *Photonics* **2022**, *9*, 788; b) E. M. Dianov, *Light Sci. Appl.* **2012**, *1*, e12.
[45] a) B. Gu, F. Yang, L. Shen, S. Zhou, S. Wang, S. Wang, *Photonics* **2023**, *10*, 136; b) Y. Li, B. Zhou, L. Zhang, S. He, *Opt. Commun.* **2015**, *344*, 156.
[46] T. Omiya, M. Yoshida, M. Nakazawa, *Opt. Express* **2013**, *21*, 2632.
[47] a) C. Zhang, Y. Yang, C. Wang, C. Liao, Y. Wang, *Opt. Express* **2016**, *24*, 3981; b) M. Wang, K. Zhao, J. Wu, Y. Li, Y. Yang, S. Huang, J. Zhao, T. Tweedle, D. Carpenter, G. Zheng, Q. Yu, K. P. Chen, *Int. J. Extrem. Manuf.* **2021**, *3*, 025401.
[48] Z. E. Ross, B. Idini, Z. Jia, O. L. Stephenson, M. Zhong, X. Wang, Z. Zhan, M. Simons, E. J. Fielding, S.-H. Yun, E. Hauksson, A. W. Moore, Z. Liu, J. Jung, *Science* **2019**, *366*, 346.
[49] a) D. Stellinga, D. B. Phillips, S. P. Mekhail, A. Selyem, S. Turtaev, T. Čižmár, M. J. Padgett, *Science* **2021**, *374*, 1395; b) Z. Wen, Z. Dong, Q. Deng, C. Pang, C. F. Kaminski, X. Xu, H. Yan, L. Wang, S. Liu, J. Tang, W. Chen, X. Liu, Q. Yang, *Nat. Photonics* **2023**, *17*, 679.
[50] Q. Li, M. Chambonneau, M. Blothe, H. Gross, S. Nolte, *Appl. Opt.* **2021**, *60*, 3954.
[51] K. Y. Lau, S. Firstov, Y. Cui, X. Liu, F. Afanasiev, J. Qiu, *J. Lightwave Technol.* **2023**, *41*, 6383.